Layered-to-tunnel structure transformation and oxygen redox chemistry in $LiRhO_2$ upon Li-extraction and insertion

Layered-to-tunnel structure transformation and oxygen redox chemistry in $LiRhO_2$ upon Li-extraction and insertion

Daria Mikhailova[1,2,3*], Olesia M. Karakulina[4], Dmitry Batuk[4], Joke Hadermann[4], Artem M. Abakumov[4,5], Markus Herklotz[2], Alexander A. Tsirlin[6,7], Steffen Oswald[2], Lars Giebeler[2], Marcus Schmidt[3], Jürgen Eckert[8,9], Michael Knapp[1], Helmut Ehrenberg[1]

1-*Karlsruhe Institute of Technology (KIT), Institute for Applied Materials (IAM), Hermann-von- Helmholtz-Platz 1, D-76344 Eggenstein-Leopoldshafen, Germany*
2-*IFW Dresden, Institute for Complex Materials, Helmholtzstr. 20, D-01069 Dresden, Germany*
3-*Max Planck Institute for Chemical Physics of Solids, Nöthnitzer Str. 40, D-01187 Dresden, Germany*
4-*EMAT, University of Antwerp, Groenenborgerlaan 171, B-2020 Antwerp, Belgium*
5-*Skoltech Center for Electrochemical Energy Storage, Skolkovo Institute of Science and Technology, 143026 Moscow, Russia*
6-*National Institute of Chemical Physics and Biophysics, Akadeemia tee 23, 12618 Tallinn, Estonia*
7-*Experimental Physics VI, Center for Electronic Correlations and Magnetism, University of Augsburg, Universitaetsstr. 1, 86159 Augsburg, Germany*
8-Erich Schmid Institute of Materials Science, Austrian Academy of Sciences, Jahnstraße 12, A-8700 Leoben, Austria
9-Department Materials Physics, Montanuniversität Leoben, Jahnstraße 12, A-8700 Leoben, Austria

*- corresponding author, d.mikhailova@ifw-dresden.de

Abstract

Layered $Li(M,Li)O_2$ (M – transition metal) ordered rock salt-type structures are used in advanced metal-ion batteries as one of the best hosts for the reversible intercalation of Li ions. Besides the conventional redox reaction involving oxidation/reduction of the M cation upon Li extraction/insertion, creating oxygen-located holes due to the partial oxygen oxidation increases capacity while maintaining the oxidized oxygen species in the lattice through high covalency of the M-O bonding. Typical degradation mechanism of the $Li(M,Li)O_2$ electrodes involves partially irreversible M cation migration towards the Li positions resulting in gradual capacity/voltage fade. Here, using $LiRhO_2$ as a model system (isostructural and isoelectronic to $LiCoO_2$), we for the first time demonstrate an intimate coupling between the oxygen redox and M cation migration. A formation of the oxidized oxygen species upon electrochemical Li extraction coincides with transformation of the layered $Li_{1-x}RhO_2$ structure into the γ-MnO_2-type rutile-ramsdellite intergrowth $Li_yRh_3O_6$ structure with rutile-like [1x1] channels along with bigger ramsdellite-like [2x1] tunnels through massive and concerted Rh migration towards the empty positions in the Li layers. The oxidized oxygen dimers with the O-O distances as short as 2.26 Å are stabilized in this structure via the local Rh-O configuration reminiscent to that in the μ-peroxo-μ-hydroxo Rh complexes. The $Li_yRh_3O_6$ structure is remarkably stable upon electrochemical cycling illustrating that proper structural implementation of the oxidized oxygen species can open a pathway towards deliberate employment of the anion redox chemistry in high capacity/high voltage positive electrodes for metal-ion batteries.

Introduction

Layered oxides based on or derived from the α-$NaFeO_2$ structure belong to the most promising positive electrode materials for Li-ion batteries [1]. The simplest $LiMO_2$ crystal structure is formed by alternating layers of MO_6 octahedra and Li ions. Although one of these materials, $LiCoO_2$, is nowadays used in commercial products, its capacity is limited by the structural instability upon extraction of more than 0.5-0.6Li per formula unit. Large variety of the layered $LiMO_2$ oxides with different cationic combinations on the M site has been tested as potential cathode materials in order to overcome these limitations. The most intriguing combination arises from a replacement of a part of Co^{3+} with Ni^{2+} and Mn^{4+} simultaneously with insertion of extra Li onto the M site that results in the chemical compositions such as xLi_2MnO_3+(1-x)$LiMn_{1/3}Ni_{1/3}Co_{1/3}O_2$ (so-called "Li-rich materials"). These materials can demonstrate anomalously high capacity up to ~300 mAh/g [2], attributed to combined cationic and anionic redox reactions, where also oxide anions are partially oxidized [3-7].

The oxygen-confined redox activity is generally associated with a strong covalency of the M – O bonding and significant contribution of O2p states to the bands near the Fermi level [8]. The experiments on the model compounds with M = Ru with strong hybridisation of the Ru4d-O2p states put forward a representation of the partially oxidized oxygen species as "peroxo"-like groups with shortened O-O distances of ~2.3 – 2.4 Å as derived from DFT calculations [9-11]. This shortening of the O-O distances can also be considered as a cooperative deformation of the oxygen pattern of the MO_6 layers driving the MO_6 octahedra towards trigonal prisms [10, 12].

As oxidation of the oxygen sublattice significantly affects the O-O interatomic distances, one may expect that it also might alter the diffusion pathways for cations and activation energies for the cation migration between the vacant Li and M positions in the charged state. In the $Li_2Ru_{0.75}Ti_{0.25}O_3$ electrode charged to 4.6 V (high enough potential to enable oxygen redox process) the M cations massively migrate to the vacant octahedral positions in the Li layers and almost reversibly return back upon discharge to 2 V. Upon numerous charge/discharge cycles part of the Ti cations remains trapped in the tetrahedral interstices between the Li and MO_6 layers that is considered as an origin of the voltage decay in these layered materials [11]. Taking into account such a detrimental effect of even small irreversibility of the cation migration, its coupling to the oxygen redox reactions become an intriguing subject for

deeper investigation as it may shed light on the possibilities to improve the performance of the high voltage positive electrode materials for the Li-ion batteries.

In the present work, we selected $LiRhO_2$ to demonstrate the intimate coupling between the oxygen redox and the cation migration. We show on the $LiRhO_2$ example that layered Li*M*O_2 oxides with the α-$NaFeO_2$ structure and *M* being a 4*d* cation hide much more surprises upon delithiation as it was assumed until now. Upon deep Li-extraction from the layered $LiRhO_2$, appearance of the "peroxo-like" species is accompanied by the Rh cation migration towards empty positions in the Li layers with subsequent formation of an intergrowth rutile-ramsdellite tunnel structure $Li_yRh_3O_6$, which demonstrates excellent intercalation properties for two kinds of tunnels, rutile-type [1x1] and ramsdellite-type [2x1] ones. The unexpected structural transformation of the layered into a rutile-ramsdellite framework phase is partially reversible and involves formation of shortened Rh-O and O-O distances with the local Rh-O configuration reminiscent of that in the μ-peroxo-μ-hydroxo Rh complexes.

Results

Synthesis and electrochemical characterization of $LiRhO_2$

The pristine single-phase $LiRhO_2$ sample was synthesized in air at 950 °C. Its powder X-ray diffraction (PXRD) pattern and crystal structure are presented in Fig.S1 of the Supporting Information. $LiRhO_2$ adopts the nearly ideal α-$NaFeO_2$ structure (*R*-3*m* space group) with 5% deficiency at the Li site revealed by the Rietveld refinement (Table S1 of the Supporting Information). The electrochemical response of $LiRhO_2$ as a positive electrode (cathode) in test cells with the Li anode strongly depends on the voltage range, especially on the upper voltage limit. In the cells charged above 4.0 V vs. Li^+/Li it demonstrates a phase transformation, which can be surmised from the analysis of galvanostatic (GCPL) curves for the first and following cycles. On the first charge up to 4.1 V, the oxidative process consists of two steps at about 3.75 V and 4.0 V. In the following cycles, an additional strong oxidative process occurs already at 3.4 V (Fig. 1a). The corresponding reductive processes are at about 3.5 V and 3.1 V. The electrochemical behavior of $LiRhO_2$ is quite different if the cell is cycled between 3.0 and 3.85 V (Fig. 1b). In this case, the oxidative peak at 3.4 V does not appear in the subsequent cycles, and the charge/discharge curves nearly replicate each other. Therefore, one can assume that the process at 3.4 V during the second and following cell charges and at 3.1 V during the cell discharge is activated by the transformation

of $LiRhO_2$ at 4.0 - 4.1 V in the first cycle. The $LiRhO_2$ cathode shows stable cycling behavior for the voltage range of 1.2 - 4.1 V at least in the first fifteen cycles (Fig. 1c).

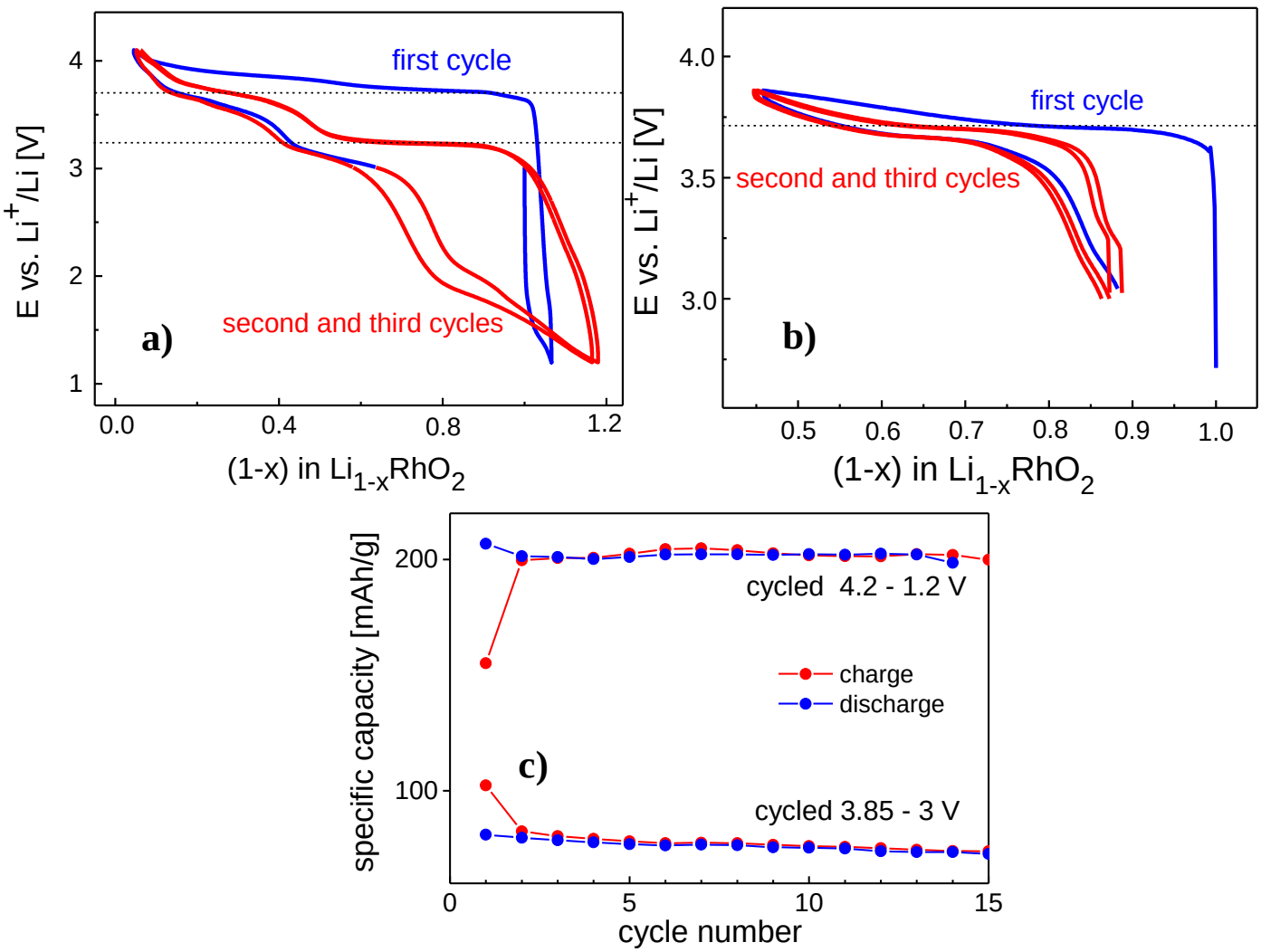

Figure 1. **a**: GCPL curves of $LiRhO_2$ cycled between 1.2 and 4.1 V vs. Li^+/Li starting with the cell discharge down to 1.2 V. About 5-6% Li can be inserted into the crystal structure at about 1.5 V. **b**: GCPL curves of $LiRhO_2$ cycled between 3.0 and 3.85 V. Total Li-amount in the sample was calculated from the current flow in the galvanostatic experiment. **c**: Specific capacity of the $LiRhO_2$ cathode cycled between 3 and 3.85 V, and between 1.2 and 4.2 V, depending on the cycle number. The current rate corresponded to extraction or insertion of 1Li during 10 h (0.1C).

A different Li-content in $Li_{1-x}RhO_2$ affects the morphology of the material, as visualized by scanning electron microscopy (SEM) images in Fig. 2. The images of half-charged $Li_{0.5}RhO_2$ are similar to those of pristine $LiRhO_2$, showing some cracks appearing in the $Li_{0.5}RhO_2$ particles. The lithium-free Li_0RhO_2 material clearly demonstrates a higher number of cracks, splitting the crystals into sheets.

The changes in the phase composition of the $LiRhO_2$ material cycled up to 3.8 and 4.1 V were monitored using PXRD data. The PXRD patterns of pristine $LiRhO_2$ and half-charged $Li_{0.5}RuO_2$ are very similar and show only a shift of the reflections due to changes in the lattice parameters, whereas the PXRD pattern of the lithium-free Li_0RhO_2 material is significantly different (see for example synchrotron PXRD patterns recorded *in situ* during electrochemical Li-extraction in Fig. 5).

An irreversible drastic change in the electrochemical behavior of $LiRhO_2$ charged above 4.0 V, together with a quite different PXRD pattern and changes in the particle morphology, indicate possible crystallographic transformation in this material upon deep Li-extraction. The quality of the PXRD patterns does not allow for *ab initio* solution of the crystal structure of the delithiated material. Therefore, we applied quantitative electron diffraction and atomic resolution scanning transmission electron microscopy imaging to reveal the crystal structure of this phase.

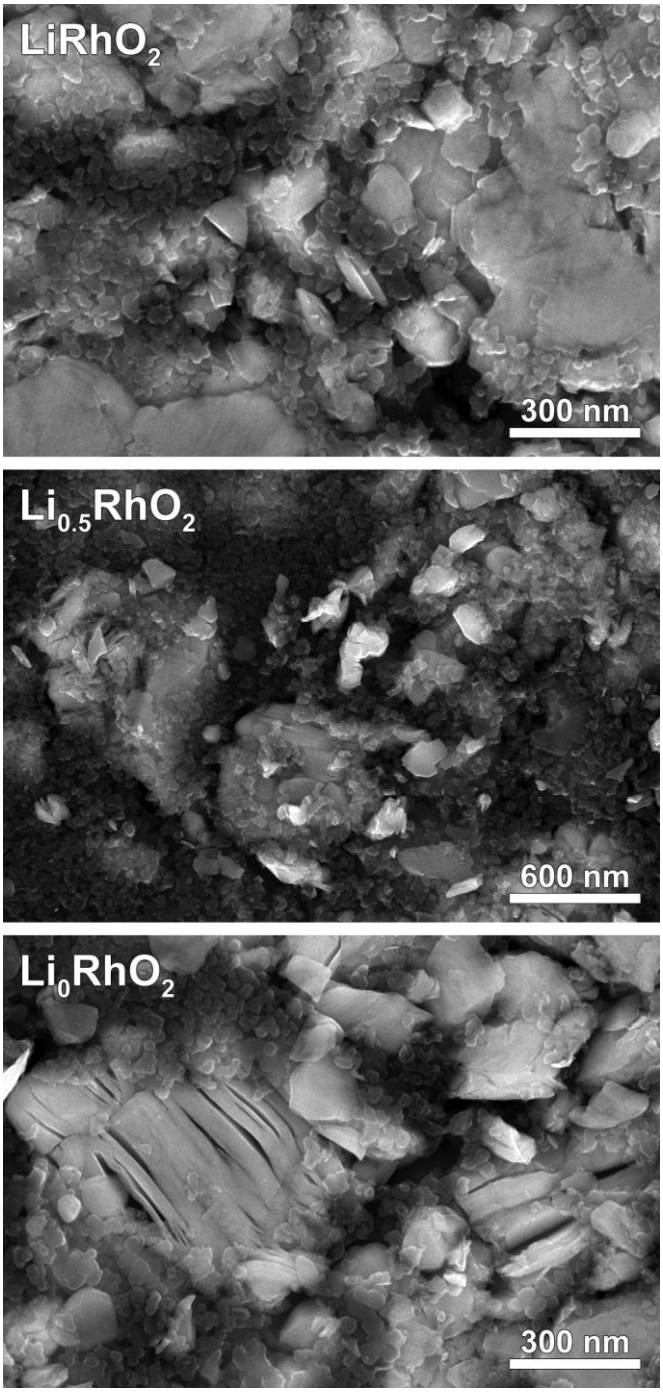

Figure 2. SEM images of the initial $LiRhO_2$ cathode mixture, and $Li_{0.5}RhO_2$ and Li_0RhO_2 cathodes after electrochemical Li-extraction.

Structure of the delithiated phase

The transmission electron microscopy (TEM) studies were done on both the chemically and electrochemically delithiated samples. The former was synthesized via reaction of stoichiometric amounts of $LiRhO_2$ and NO_2BF_4 in acetonitrile for 3 days. It demonstrates a PXRD pattern strikingly similar to that of the sample obtained by

electrochemical oxidation to 4.1 V (Fig. S2 of the Supporting Information). The reciprocal lattice of the material was reconstructed using a combination of selected area electron diffraction (SAED, Fig. S3 of the Supporting Information) and electron diffraction tomography (EDT). Both methods reveal a *C*-centered lattice with the unit cell parameters $a \approx 14.8$ Å, $b \approx 3.1$ Å, $c \approx 4.4$ Å, $\alpha, \beta, \gamma \approx 90^{\circ}$. The structure was solved using quasikinematical electron diffraction intensities extracted from EDT data. The positions of the Rh atoms were found with the charge flipping algorithm. The O positions were identified using difference Fourier maps. Initial structure solution in the *Cmmm* space group resulted in an unrealistic coordination environment for the Rh atoms. Lowering the symmetry to *C*2/*m* with the monoclinic axis *b* provided a reasonable structural model. The Li positions could not be unraveled directly from the EDT data because of their low occupancy and the low atomic number of Li. Tentative positions of the Li atoms were determined by means of Monte-Carlo-based optimization (see Experimental methods and Table S2 of the Supporting information).

In order to distinguish between the Li-deficient rhombohedral α-$NaFeO_2$-type structure and the new transformed monoclinic structure, we will further denote them as $Li_{1-x}RhO_2$ and $Li_yRh_3O_6$, respectively. The refined monoclinic structure resembles that of the mineral *nsutite*, or its synthetic analog γ-MnO_2 [13, 14]. The $Li_yRh_3O_6$ structure is based on a 1:1 intergrowth of rutile (pyrolusite-type) and ramsdellite-type fragments. The same kind of rutile-ramsdellite intergrowth structure is adopted by $Li_xTi_3O_6$ [15, 16]. The basic units of the structure are single rutile-type $Rh1O_6$ octahedral chains and double rutile-type edge-sharing $Rh2O_6$ octahedral chains, running along the *b* axis (Fig. 3a).

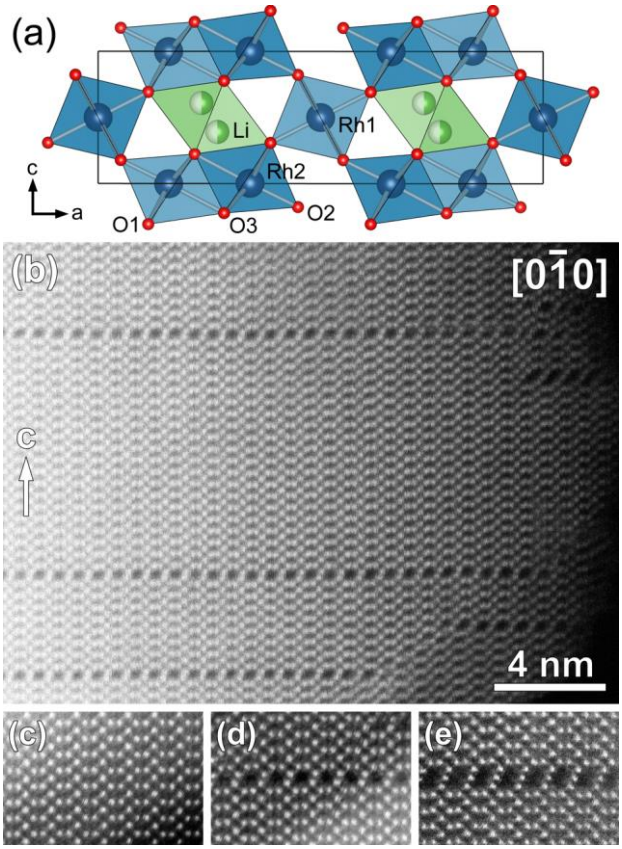

Figure 3. (a) Crystal structure of $Li_yRh_3O_6$ viewed along the *b*-axis. (b) A typical high resolution HAADF-STEM image of the structure; (c) magnified images of $Li_yRh_3O_6$ confirming the rutile-ramsdellite intergrowth structure; (d) and (e) magnified images of most abundant defects in the structure, containing hollandite-type [2x2] and psilomelane-type [2x3] tunnels, respectively.

The single $Rh1O_6$ chain connects four neighboring $Rh2O_6$ double-rutile chains together forming two types of tunnels along the *b* axis: the smaller rutile-type [1x1] tunnels and the larger ramsdellite-type [2x1] tunnels. The structural model of $Li_yRh_3O_6$ is further confirmed by aberration corrected high angle annular dark field scanning transmission electron microscopy (HAADF-STEM) imaging. The [010] HAADF-STEM image in Fig. 3b clearly demonstrates the projections of the Rh columns. The main structure motif is formed by the rutile-type [1x1] tunnels and ramsdellite-type [2x1] tunnels (Fig. 3c), in agreement with the refined structural model. However, numerous defects are present in the material, related to a formation of larger tunnels, such as hollandite-type [2x2] tunnels (Fig. 3d), psilomelane-type [2x3] tunnels (Fig. 3e) and even larger [2x4] tunnels.

***In situ* structural studies**

In order to observe continuously the structural transformation in the material in dependence on the Li-content we carried out *in situ* synchrotron powder X-ray diffraction studies of the $Li_{1-x}RhO_2$ cathode in electrochemical test cells with Li anode during first cell charge up to 4.2 V and subsequent discharge down to 1 V (Fig. 4). The crystallographic data, atomic coordinates, atomic displacement parameters and main interatomic distances for $Li_{1-x}RhO_2$ and $Li_yRh_3O_6$ obtained by the delithiation of $LiRhO_2$ at 4.06 V are presented in Tables S3 and S4 of the Supporting Information, respectively. The same data for the $Li_{1-x}RhO_2$ and $Li_yRh_3O_6$ phases after cell discharge to 1.0 V are shown in Tables S5 and S6 of the Supporting Information. The Rietveld profiles of initial $LiRhO_2$ and the materials charged to 4.06 V and discharged to 1.0 V are shown in Fig. 5.

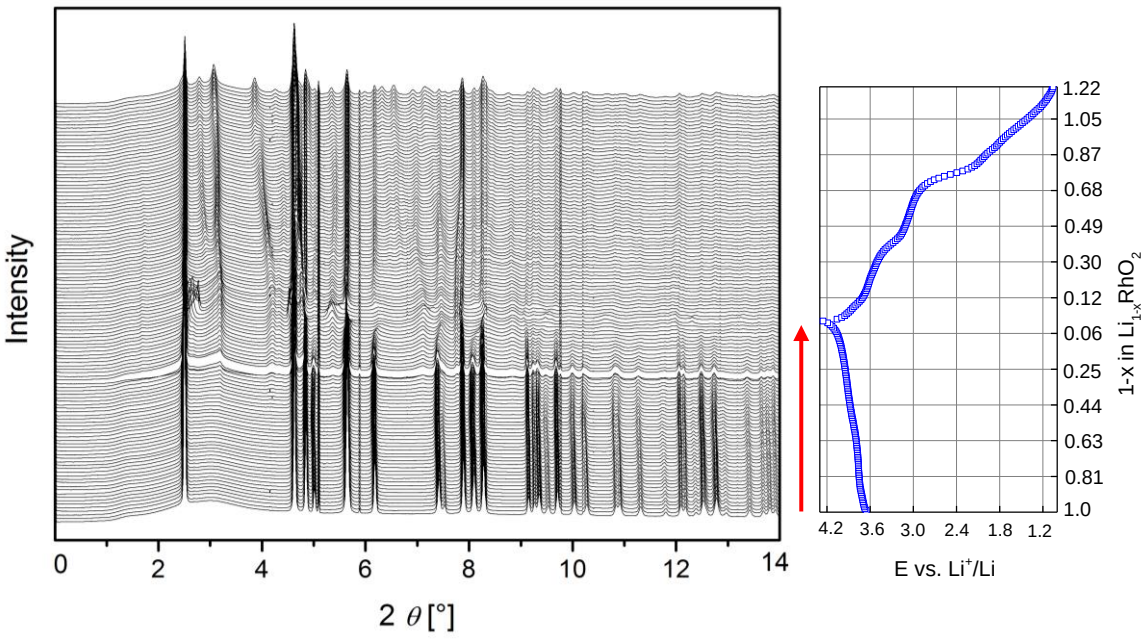

Figure 4. *In situ* synchrotron powder diffraction data from $LiRhO_2$ as cathode material in an electrochemical test cell with Li-anode during GCPL at C/10 (left), and voltage profile of the *in situ* cell vs. total Li-content in the material (right).

Electrochemical Li extraction from $Li_{1-x}RhO_2$ proceeds via a solid-solution mechanism at least for $0 \leq x \leq 0.45$ corresponding to cell voltages between 3 V and 3.8 V vs. Li^+/Li. A further increase in the cell voltage up to 4.1 V results in additional broad reflections that can only be explained by a formation of the rutile-ramsdellite intergrowth monoclinic $Li_yRh_3O_6$ structure. In rhombohedral $Li_{1-x}RhO_2$, both lattice

parameters *a* and *c* increase with decreasing Li-content (Fig. 6a). This behavior differs from the majority of the layered intercalation compounds, where the *a* parameter decreases upon Li extraction. This trend is usually explained by the shrinkage of *M*-O bonds in the MO_6 octahedra, because the *M* cation radius decreases with increasing average oxidation state [17]. On the other hand, the parameter *c* increases owing to the increased repulsion between the two neighboring oxygen layers that come into direct contact when the Li ions are removed [17]. The unusual structural behavior of $Li_{1-x}RhO_2$ can be ascribed to the weakening of the metal-metal bonding between the Rh atoms in the octahedral layers, similar to that observed in $LiNbO_2$ [18].

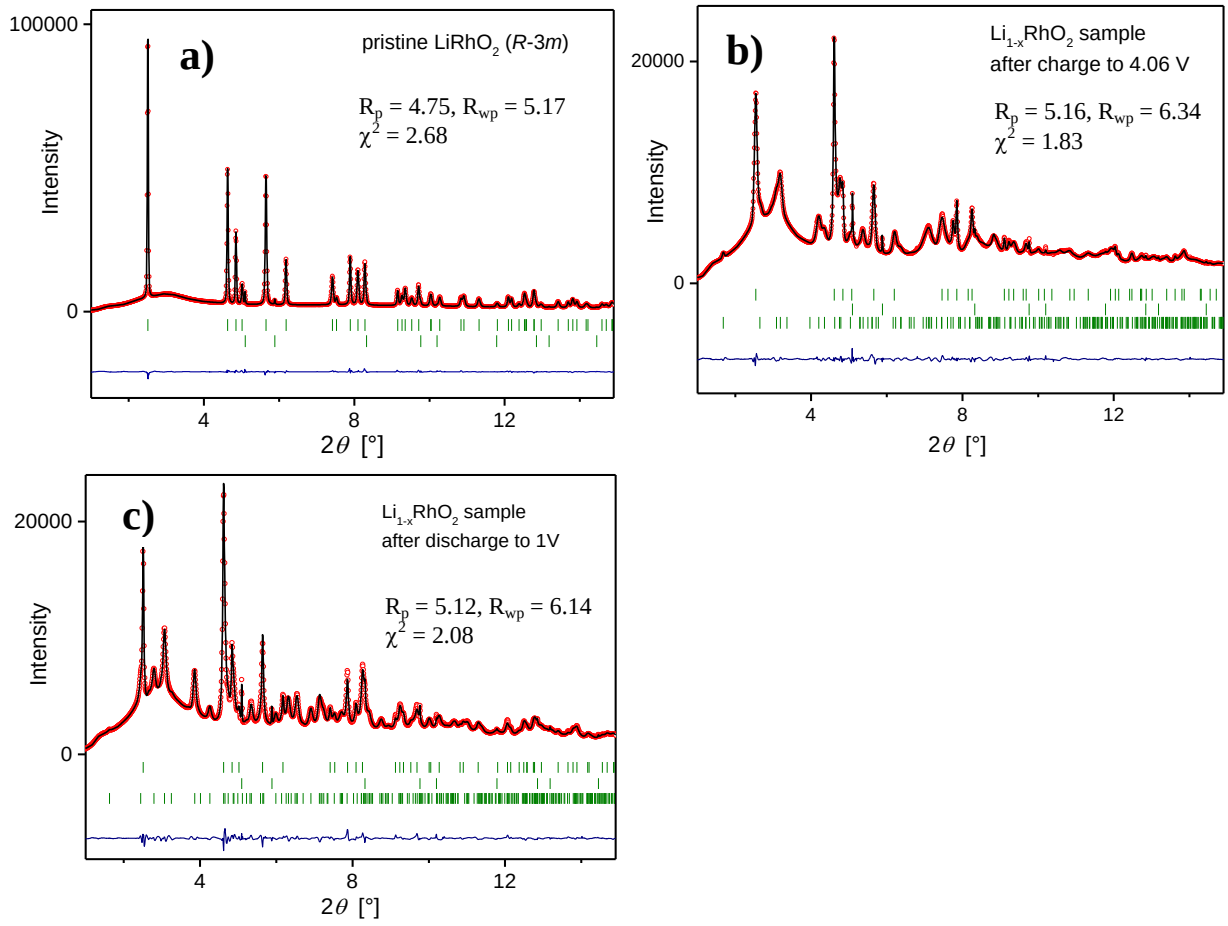

Figure 5. Synchrotron powder diffraction patterns of **a)** $Li_{1-x}RhO_2$ in the initial state, **b)** charged up to 4.06 V, and **c)** subsequently discharged down to 1V. Bragg position marks from top to bottom correspond to the reflection positions of $Li_{1-x}RhO_2$ with the *R*-3*m* symmetry, Al from the *in situ* cell, and $Li_yRh_3O_6$ with the *C*2/*m* symmetry. The total Li-content was refined to 0.06 for the fully charged sample **b)**, and 1.21 for the fully discharged one **c)**. Analysis data of structural refinements after background correction were calculated by Fullprof according to the work [29].

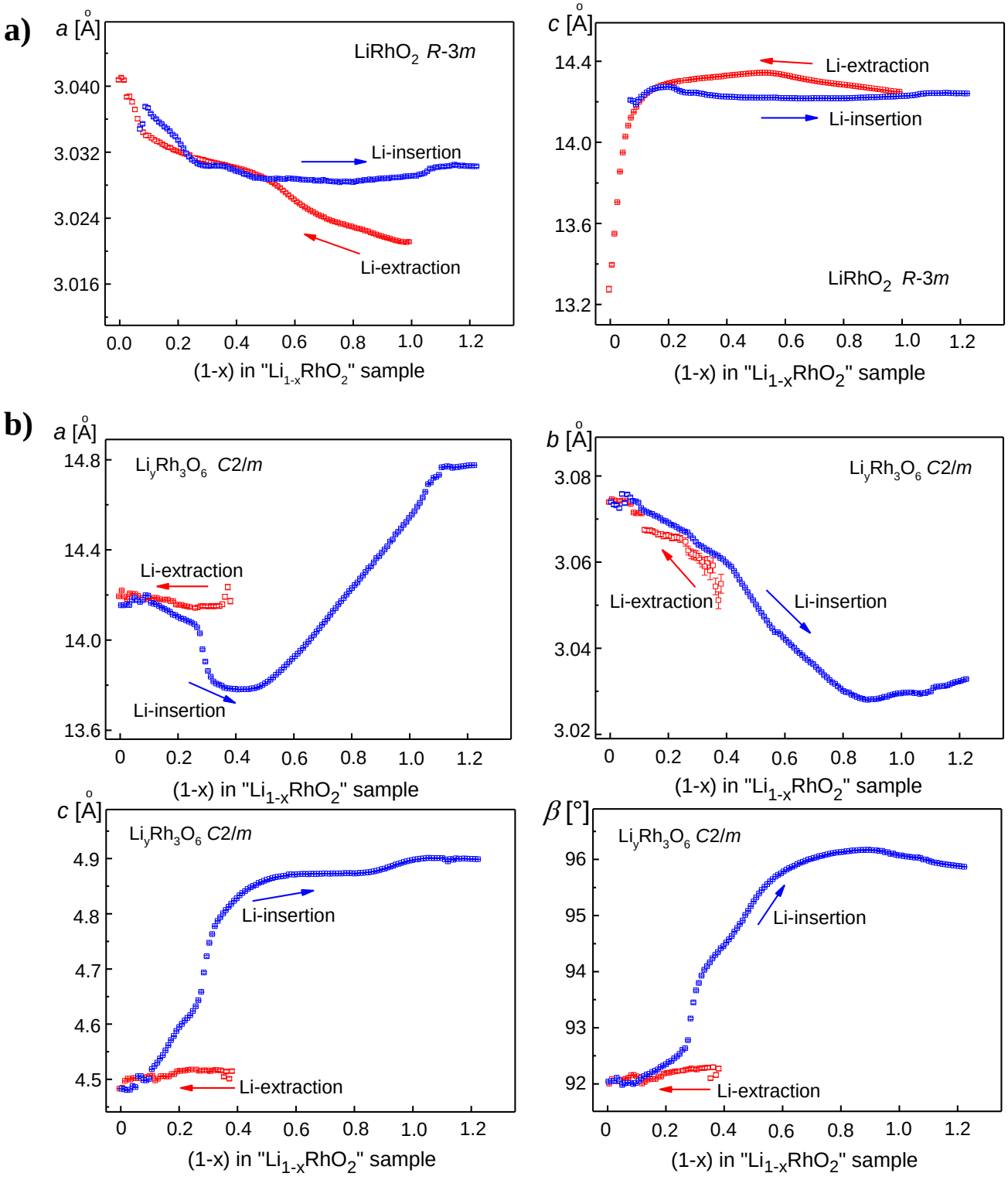

Figure 6. Evolution of the lattice parameters of **a)** rhombohedral $LiRhO_2$ and **b)** monoclinic $Li_yRh_3O_6$ depending on the Li content during electrochemical Li extraction and insertion. Total Li amount in the sample was calculated from the current flow in the galvanostatic experiment.

High quality *in situ* synchrotron powder X-ray diffraction data made it possible to calculate occupancy factors for the Li position in rhombohedral $Li_{1-x}RhO_2$. The Li content obtained by the Rietveld refinement in the single-phase region (up to $x \approx 0.45$) is in excellent agreement with the Li content calculated from the current flow in the galvanostatic electrochemical experiment (Fig. 7).

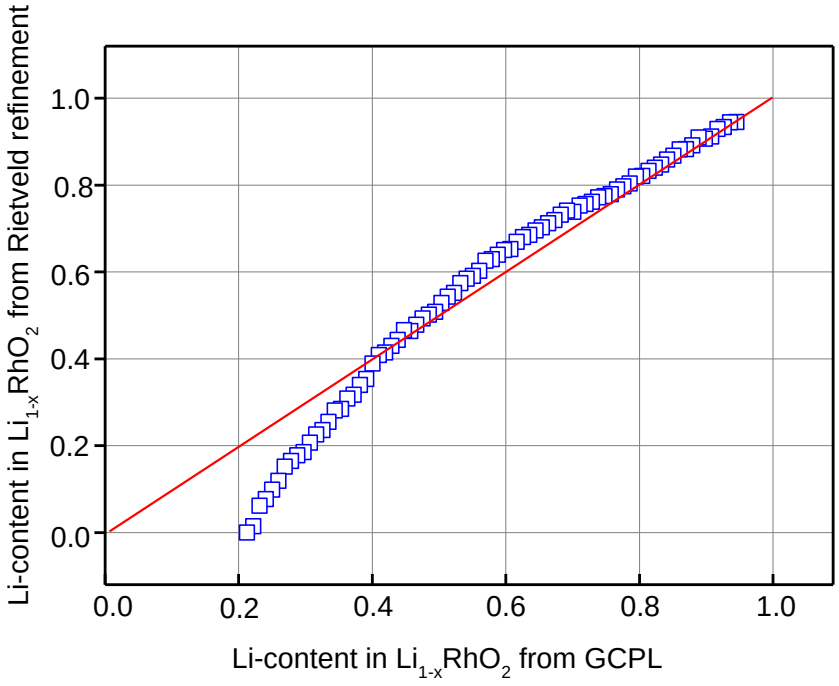

Figure 7. Correlation between Li content in the layered $Li_{1-x}RhO_2$, obtained from structure refinement (blue squares), and from the current flow in galvanostatic experiment (red line) during *in situ* synchrotron powder diffraction.

The formation of the $Li_yRh_3O_6$ phase at $x \approx 0.45$ manifests itself by a kink in the compositional dependence of the parameter *a* of $Li_{1-x}RhO_2$ (Fig. 6a). The lattice parameters *a* and *c* of the monoclinic $Li_yRh_3O_6$ phase remain nearly constant upon further delithiation of the sample, while the parameter *b* increases following the Li removal from the structure (Fig. 6b).

At high potentials, the rhombohedral layered $Li_{1-x}RhO_2$ structure transforms into monoclinic, which is indicated by an abrupt shift of the 003 reflection of the rhombohedral $Li_{1-x}RhO_2$ to larger 2θ values and by the appearance of an additional reflection at 4.77° (Fig. S4 of the Supporting information). The Rietveld refinement confirms the symmetry transformation from *R*-3*m* to *C*2/*m*, so that $Li_{1-x}RhO_2$ acquires the $LiMoO_2$-type structure [19]. At voltages above 4.1 V, corresponding to less than

1% Li in the sample, only a minor amount (about 5-7 wt.%) of the rhombohedral phase remains. This phase transition is reversible. Upon cell discharge, the *C*2/*m* $Li_{1-x}RhO_2$ structure completely transforms back into the rhombohedral one at 3.7 V, which corresponds to about 6% Li in the material.

Upon lithiation of the fully charged material, a fraction of the $Li_yRh_3O_6$ phase transforms back into the layered $Li_{1-x}RhO_2$ structure. The weight ratio between these phases becomes 1:1 at x = 0.9 and remains constant during further Li insertion. According to the current flow values in the *in situ* galvanostatic experiment, the material accommodates Li up to a total Li:Rh ratio of 1.2. This amount is slightly larger than the amount of Li removed during the charging process, which suggests that not only large ramsdellite-type [2x1] tunnels, but also small rutile-type [1x1] tunnels support the intercalation of the Li ions. Indeed, the ramsdellite-type tunnels can accommodate Li only up to the Li:Rh = 2/3 ratio. We also observed a strong change in the lattice parameters of $Li_yRh_3O_6$ below 3.15 V, especially in the parameter *a*, which we relate to Li entering the rutile-type tunnels. The Li insertion into rutile-type structures primarily affects the cell dimensions in the directions perpendicular to the tunnels. For example, in the TiO_2 rutile structure a pronounced increase in the parameter *a* was observed [20]. It is also worth to note that the rhombohedral $Li_{1-x}RhO_2$ phase is electrochemically inactive below 3.15 V, which is suggested by nearly constant lattice parameters during further cell discharge. The structural features of the pristine material and the layered $Li_{1-x}RhO_2$ after cell discharge down to 1 V are also very similar confirming the electrochemical inactivity below 3.15 V. The Rh-O bond in the rhombohedral $Li_{1-x}RhO_2$ (Fig. 8) reveals only minor shrinkage during cell charging, in spite of the noticeable difference between the ionic radii of Rh^{3+} (0.665Å) and Rh^{4+} (0.60Å) [21]. At the same time, the nearest-neighbor oxygen-oxygen distance decreases. In the subsequent cell discharge, both interatomic distances reached their initial values. A similar shortening of the Rh-O and O-O bonds is observed in the $Li_yRh_3O_6$ phase. After electrochemical charge to 4.06 V it exhibits one very short Rh-O bond of 1.65 Å and several shortened O–O distances of 2.26-2.50 Å compared to 2.8-2.9 Å in conventional oxide materials and to the sum of the ionic radii of two O^{2-} anions (r = 1.4 Å [21]). In contrast, the structural model at 1 V does not feature any shortened bonds.

The unusual shortening of the O-O interatomic distances in the structures delithiated electrochemically above ~4 V might indicate an extra covalent bonding between the oxygen atoms due to a partial redox process in the oxygen sublattice eliminating electrons from σ* antibonding states of the O-O dimers [8]. X-ray photoelectron spectroscopy is a sensitive tool to detect redox processes on the oxygen ions.

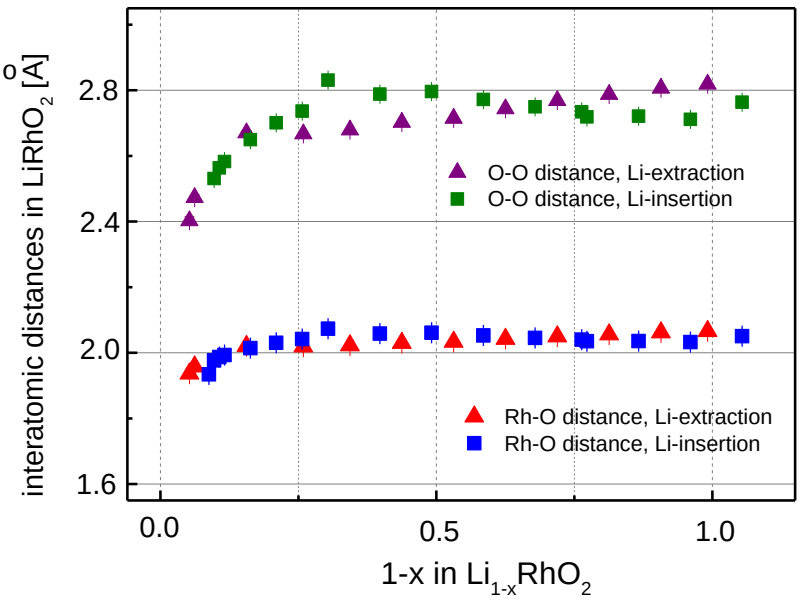

Figure 8. Evolution of Rh-O and O-O interatomic distances in the rhombohedral $Li_{1-x}RhO_2$ during Li-extraction and subsequent Li-insertion. The Li-content in the material was calculated from the current flow in the GCPL measurement.

Evidence for anionic redox process

The X-ray photoelectron spectroscopy (XPS) studies of pristine $LiRhO_2$ and Li-extracted $Li_{0.5}RhO_2$ and Li_0RhO_2 samples (Fig. 9) revealed very similar Rh3d spectra with practically no shift towards higher binding energy (BE) for delithiated samples as it would be expected for an increased oxidation state of Rh [22, 23]. The absence of any noticeable variation of the Rh oxidation state is in line with the minor variation of the Rh-O interatomic distances upon delithiation. In contrast to the Rh3d spectra, the O1s spectra of these materials substantially differ from each other. The O1s spectrum of pristine $LiRhO_2$ shows a well-defined peak at 529.3 eV, which is characteristic for O^{2-} ions in the structural network of oxides [24]. The second less-intense peak at 531.1 eV can be attributed to subsurface O^- species, which arise mostly from some deficiencies in the subsurface of the transition metal oxide [24]. The intensity of this peak becomes somewhat higher after the full oxidation of $LiRhO_2$. The lattice O^{2-} -

peak is shifted to smaller binding energies after half- and full-oxidation, which reflects the structural rearrangement upon increasing the Li deficiency. Additionally, two new peaks appear in the spectra of $Li_{0.5}RhO_2$ and Li_0RhO_2. The first one at 533.0 eV is weak in $Li_{0.5}RhO_2$ and more intense in Li_0RhO_2. It is usually associated with the products of electrolyte oxidation [9, 25, 26]. The second peak at 529.8 eV also increases from $Li_{0.5}RhO_2$ to Li_0RhO_2.

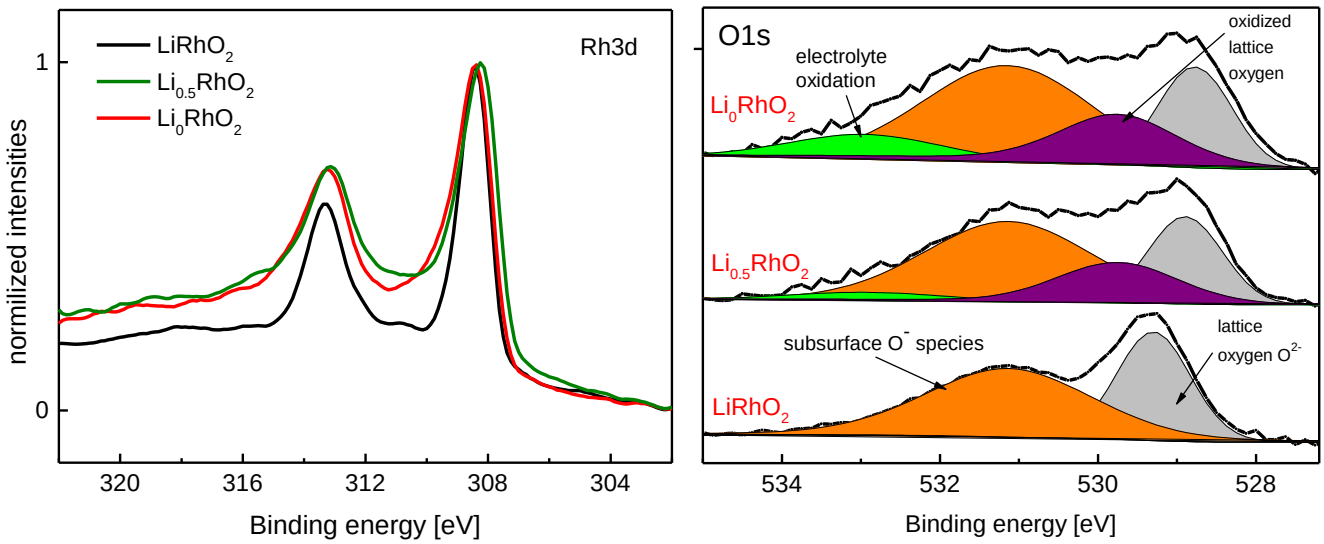

Figure 9. Rh3d (left) and O1s (right) spectra of pristine $LiRhO_2$, $Li_{0.5}RhO_2$ and Li_0RhO_2 after electrochemical Li-extraction. The O1s spectrum of pristine $LiRhO_2$ consists of two peaks at 529.3 eV and 531.1 eV, which correspond to O^{2-} ions of the structural network, and O^- ions because of some cation deficiency in the subsurface region. The fully delithiated material contains two additional oxygen components. The peak at 533.0 eV is attributed to products of electrolyte oxidation, while the peak at 529.8 eV corresponds to the oxidized lattice oxygen, according to [24]. Note that the lattice O^{2-} peak is shifted to a lower BE in the delithiated material, reflecting the structural phase transition.

Recent literature ascribes the oxygen component at around 530 eV to the formation of "peroxo"-like species in transition metal oxides. This conjecture stems from the fact that occupied states in the vicinity of the Fermi level are largely formed by O2p ions. Upon Li removal from the structure, holes are formed on both oxygen anions and transition metal cations. For example, detailed XPS studies of $LiCoO_2$ upon lithium deintercalation showed simultaneous partial oxidation of cobalt and oxygen [25]. The presence of an additional oxygen component located at ~530.5 eV was detected in $Li_2Ru_{0.5}Mn_{0.5}O_3$ [26] and $Li_2Ru_{0.5}Sn_{0.5}O_3$ [9] after Li deintercalation. Note that in these materials ruthenium ions were oxidized together with oxygen, which was

concluded from the shift to the higher binding energies of the $Ru3p_{1/2}$, $Ru3p_{3/2}$ and $Ru3d_{5/2}$ core peaks after delithiation. In contrast to that, from our XPS data one can conclude that rhodium ions, at least in the surface region, remain mostly unaffected by the lithium extraction. Charge compensation must occur via anionic redox processes, in accordance with the contracted oxygen-oxygen distances in both rhombohedral $Li_{1-x}RhO_2$ and monoclinic $Li_yRh_3O_6$ compounds after Li extraction.

Energetics and stability of Li_xRhO_2

The stability of different structures formed upon Li deintercalation from $Li_{1-x}RhO_2$ was assessed by density-functional band-structure calculations. The total energies of different crystal structures depending on the Li content are shown in Fig. 10. For x = 0, the layered α-$NaFeO_2$ phase has the lowest energy. However, around x = 1/3 the $Li_yRh_3O_6$-type structure becomes similar in energy, while at x = 1 the $Li_yRh_3O_6$-type structure becomes nearly 0.5 eV/f.u. lower in energy than the layered α-$NaFeO_2$ one. Assuming that the α-$NaFeO_2$-type lithiated phase transforms into the $Li_yRh_3O_6$-type delithiated phase, we estimate the corresponding redox potential as the energy difference between these two structures minus the energy of metallic Li (~1.9 eV) which yields E ~ 3.1 V in reasonable agreement with the experiment, where the redox processes span a potential range between 3 V and 4 V.

We also considered the stability of the spinel structure that turns out to be unstable both at x = 0 and x = 1. However, this structure becomes stable around x = 0.5, where the optimal composition of $LiRh_2O_4$ is reached. This suggests that the spinel structure may form during the intercalation process, but it is not a stable structure for either of the lithiated or delithiated forms.

Relaxed crystal structures of the $Li_yRh_3O_6$-type phases at different Li content give insight into the spatial arrangement of the Li ions. The Li atoms in the ramsdellite-type tunnels feature tetrahedral coordination with two pairs of Li–O distances of 1.81 Å and 2.05 Å, respectively. The Li atoms in the rutile-like tunnels adopt the tetrahedral coordination as well, with Li–O distances of 1.85 Å and 1.92 Å, respectively.

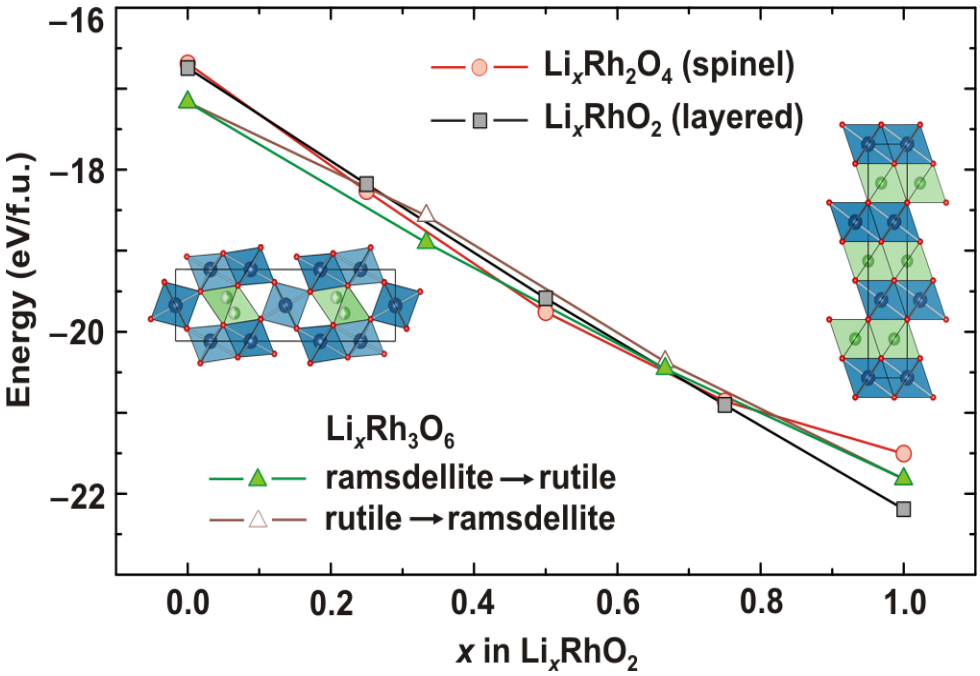

Figure 10. Total energies of different structure types (α-$NaFeO_2$-type layered, spinel, and $Li_yRh_3O_6$) depending on the Li content x. For the $Li_yRh_3O_6$-type structure, open and closed symbols denote different sequences of the filling of structural tunnels: the rutile-type tunnels are filled after the ramsdellite-type ones (filled symbols), or the other way around (open symbols).

The comparison of the total energies for the same $Li_yRh_3O_6$-type structure but with different occupied Li positions shows that filling of ramsdellite-type tunnels is energetically favorable in the beginning of the intercalation process. However, at x = 1/3 the two possible structures (one with fully filled ramsdellite-type tunnels and empty rutile-type tunnels, and the other one with half-filled ramsdellite-type tunnels and fully filled rutile-type tunnels) have nearly the same energy. Therefore, the filling of rutile-type tunnels becomes feasible as soon as the ramsdellite-type tunnels are at least partially filled. The transformation back into the α-$NaFeO_2$-type structure would be energetically even more favorable, but it may be impeded by kinetic effects.

Discussion

$LiRhO_2$ demonstrates a very complex behavior upon electrochemical Li extraction/insertion. Upon charge to 3.85 V, up to 0.55 Li can be removed with a sloped charge curve and only 0.45 Li are inserted back upon discharge to 3.0 V. Further charge-discharge cycles demonstrate good capacity retention with a reversible capacity value of ~90 mAh/g and an S-shaped charge-discharge curve indicating a

solid solution mechanism. Layered $Li_{1-x}RhO_2$ with the α-$NaFeO_2$ structure cycles reversibly in this voltage range (see Figure S5 of the Supporting Information).

However, the most spectacular transformation occurs when $LiRhO_2$ is charged to 4.1 V, losing practically all Li. The subsequent discharge proceeds with two plateaus at ~3.5 V and ~3.1 V, which remain in the charge and discharge curves during the further cycles. The material charged to 4.1 V exhibits highly reproducible electrochemical activity in the 1.2 – 4.1 V potential range taking up to 20% more Li compared to the initial $LiRhO_2$ composition and resulting in a sustainable capacity of ~ 200 mAh/g, which is slightly larger than its theoretical capacity of 189 mAh/g assuming the redox process with one electron per formula unit.

As revealed by TEM and powder X-ray diffraction, extraction of more than ~0.5 Li from the layered $Li_{1-x}RhO_2$ structure triggers a dramatic phase transformation. The 2D layered $Li_{1-x}RhO_2$ structure converts into the 3D $Li_yRh_3O_6$ framework structure, which can be represented as an intergrowth of rutile and ramsdellite, which are built of the chains of edge-sharing RhO_6 octahedra embracing the [1x1] (rutile-type) and [2x1] (ramsdellite-type) tunnels. The transformation of the layered structure to the framework structure requires a massive rearrangement of the Rh cations. Although TEM demonstrates the presence of planar defects in $Li_yRh_3O_6$, the structure appears to be relatively well ordered indicating that the Rh migration occurs in a concerted way. The mechanism of this transformation should involve a cooperative movement of the Rh atoms that occurs without long-range diffusion. HAADF-STEM data from the interface regions between the layered and the framework structures provide information to deduce such a mechanism (Fig. 11). Remarkably, in most cases the structures intergrow by sharing single rutile-type octahedral chains; and the layered structure demonstrates significant deformation of the (RhO_2) octahedral layers in vicinity of the interface. Also, these intergrowths establish a very specific orientation relationship between the structures, with the (RhO_2) octahedral layers of the layered structure being parallel to the (201) planes of the framework structure, and this relationship is observed in all investigated crystals (Fig. S6 of the Supporting Information).

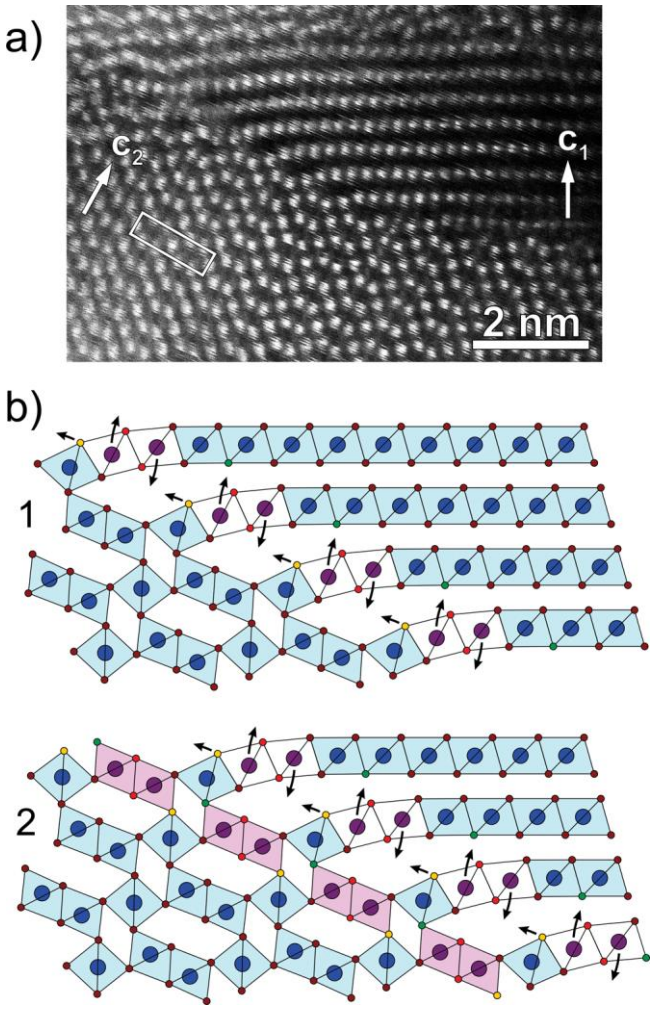

Figure 11. (a) HAADF-STEM image showing typical intergrowth of the layered $Li_{1-x}RhO_2$ and framework $Li_yRh_3O_6$ structures. The white rectangle marks the unit cell of the framework structure, while c_1 and c_2 represent the crystallographic *c* axes in the layered and framework structures, respectively. (b) Schematic illustration of the transformation of the layered structure into the framework structure. Blue and purple circles represent Rh atoms, which are coordinated by oxygen octahedra of various colors. The Li atoms are not shown for clarity. The transformation of the layered structure into the framework structure relies on rotation of fragments of double Rh atoms (purple) and double O atoms (bright red) in the octahedra marked in white.

Analyzing the atomic arrangement of Rh and O along the (201) planes, one finds a striking similarity with that of the (RhO_2) layers in the parent layered structure, thus confirming our conjecture that the structural transformation requires only a minor short-range rearrangement of the atoms. We infer that this transformation involves a cooperative rotation of the 2Rh-2O chains (purple Rh species and bright red O species in Fig. 11b). The proposed mechanism also explains the formation of tunnels of any

2×n dimensions, i.e. n = 1 is demonstrated in Fig. 11b and n = 2 in Fig. S6 of the Supporting Information.

The ramsdellite-rutile intergrowth $Li_yRh_3O_6$ phase is a perfect host structure for Li insertion and extraction, because it allows Li intercalation not only into larger ramsdellite-type tunnels but also into smaller rutile-type tunnels, while isostructural γ-MnO_2 accommodates Li cations only in the ramsdellite-type tunnels. To the best of our knowledge, there are no other examples among complex oxides with the γ-MnO_2-type structure, which can reversibly intercalate so much Li^+ in both types of tunnels.

$LiCoO_2$ and $LiRhO_2$ are isostructural, and the Co^{3+} ($3d^6$) and Rh^{3+} ($4d^6$) cations are isoelectronic. This apparent similarity could result in similar deintercalation behavior. However, the layered structure persists in the whole compositional range of $Li_{1-x}CoO_2$, whereas layered $LiRhO_2$ transforms into the framework-type $Li_yRh_3O_6$ structure upon deintercalation.

A comparison of $LiCoO_2$ and $LiRhO_2$ nicely illustrates the difference between Co3d-O2p and Rh4d-O2p hybridization on the structural behaviour of the layered positive electrode materials. The metal-oxygen hybridization controls the involvement of oxygen in the redox process, which, in turn, may couple to structural transformations, because the removal of electrons from oxygen should stabilize short O–O distances.

The remarkable feature is that the onset of the structure transformation in $Li_{1-x}RhO_2$ roughly coincides with appearance of the peroxo-like oxygen species detected by XPS. It is tempting to assume that the driving force behind the $Li_{1-x}RhO_2$-$Li_yRh_3O_6$ transformation could be related to proper accommodation of this peroxo species due to short O-O contacts (up to 2.26 Å) between the oxygen atoms of the double and single rutile-type octahedral chains.

Although the direct comparison of the molecular peroxo complexes and peroxo-like species in the crystal lattice might not be straightforward, one can notice a remarkable analogy between the local configuration of the Rh-O bonding in $Li_yRh_3O_6$ and peroxo-bridged dimeric species $[(NH_3)_4Rh(O_2)(OH)Rh(NH_3)_3(H_2O)]^{3+}$ [26]. This μ-peroxo-μ-hydroxo complex consists of two $Rh(O,N)_6$ octahedra linked together through an oxygen atom of the OH- group and O_2^{2-} peroxogroup with the O-O distance of 1.49 Å, together forming a twisted five-membered ring (Fig. 12c). Similar five-membered rings connecting two RhO_6 octahedra can be identified in the

$Li_yRh_3O_6$ structure (Fig. 12a,b). However, the interatomic distance in the "peroxo"-like group in $Li_yRh_3O_6$ is much longer (2.26 Å) than the usual O-O separation of ~1.5 Å in the O_2^{2-} peroxo-group indicating that the short O-O contact in $Li_yRh_3O_6$ is not necessarily a sign of a covalent bond. Nevertheless, one can suppose that the lower energy of the $Li_yRh_3O_6$ phase compared to the layered Li_xRhO_2 phase at low Li content is associated with extra bonding between the Rh atoms and O_2^{n-} groups. This covalent bonding is regarded as a necessary prerequisite for a reversible anionic redox chemistry without release of O_2 gas [7]. Further study of chemical bonding in deintercalated $Li_yRh_3O_6$ will be insightful.

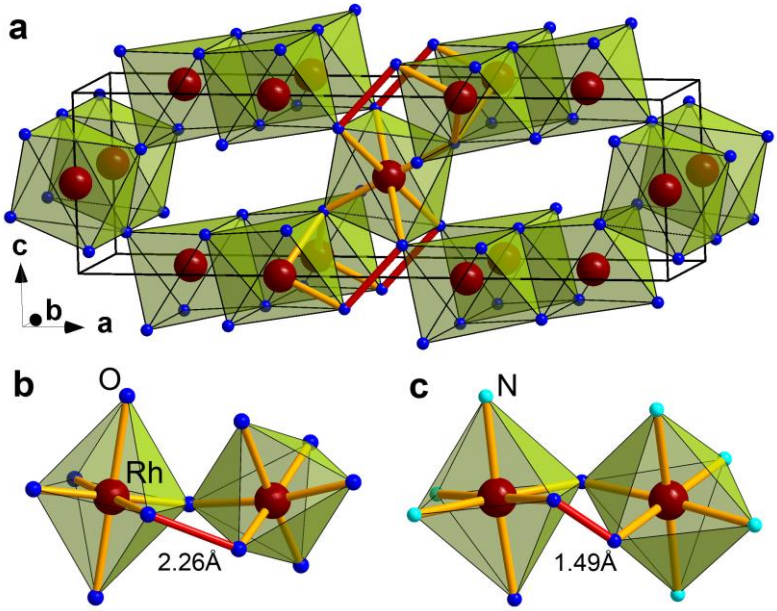

Figure 12. Comparison of the Rh coordination environment in $Li_yRh_3O_6$ **(a, b)** and μ-peroxo-μ-hydroxo complex $[(NH_3)_4Rh(O_2)(OH)Rh(NH_3)_3(H_2O)]^{3+}$ **(c)**. The short O-O bonds are marked in red. Li atoms are not shown for clarity.

Conclusion

Layered $LiRhO_2$ demonstrates an unique behavior upon chemical or electrochemical delithiation as a positive electrode material in Li-ion batteries. When charged above 4.0 V, it exhibits massive, concerted and partially reversible migration of Rh cations towards empty octahedral positions in the Li layers resulting in the $Li_yRh_3O_6$ phase with a rutile-ramsdellite intergrowth structure. The Rh cation migration is accompanied by the anionic redox process, and oxygen dimers with short O-O separations of 2.26 Å are formed. Their configuration in the deintercalated $Li_yRh_3O_6$ structure is reminiscent of that in the μ-peroxo-μ-hydroxo complex of Rh(III).

Surprisingly, the transformed structure can accept significantly more Li compared to the layered $LiRhO_2$ due to the population of both ramsdellite and rutile-type tunnels with Li atoms. Upon lithiation of the fully delithiated material, a fraction of the $Li_yRh_3O_6$ phase transforms back into the layered $Li_{1-x}RhO_2$ structure resulting in the weight ratio between these phases of 1:1 at the total Li amount in the material of 10%. The phase ratio remains constant during further Li insertion.

Experimental methods

Synthesis, phase analysis and thermal stability studies

$LiRhO_2$ samples were prepared by solid state reaction from stoichiometric amounts of Li_2CO_3 (Alfa Aesar, 99.9%) and Rh_2O_3 (Alfa Aesar, 99.95%) placed in Al_2O_3 crucibles at 950°C for 24 h. Li-deficient $Li_{1-x}RhO_2$ samples were obtained in electrochemical cells. Alternatively, the deeply delithiated sample was produced via a chemical reaction at room temperature under Ar atmosphere in acetonitrile medium between $LiRhO_2$ powder and nitronium tetrafluoroborate, NO_2BF_4, as an oxidizing agent. Then, $Li_{1-x}RhO_2$ samples were washed with acetonitrile to remove traces of unreacted agents and dried under vacuum at room temperature.

Phase analysis and determination of cell parameters of $LiRhO_2$ at room temperature were carried out using X-ray powder diffraction (XPD) with a STOE STADI P diffractometer (Cu-$K\alpha_1$-radiation, λ = 1.54059 Å) in transmission mode. Diffraction experiments for phase analysis of lithium-deficient $Li_{1-x}RhO_2$ materials after electrochemical treatments or chemical oxidizing were performed without any contact of the sample with air.

Electrochemical characterization

Electrochemical studies on $LiRhO_2$ cathodes were performed with a VMP3 (Biologic, France) multichannel potentiostatic-galvanostatic system in standard Swagelok-type cells with metallic Li as anode material. For the positive electrode a mixture of $LiRhO_2$, carbon black and polyvinylidene difluoride (PVDF) as polymer binder in an 80:10:10 weight ratio was pressed on Al-meshes with 8 mm diameter and dried in vacuum at 353 K. A 1M solution of $LiPF_6$ in a mixture of ethylene carbonate (EC) and dimethylcarbonate (DMC) (1:1) was used as electrolyte (LP30, BASF). The cells were assembled in an Ar-filled glovebox with H_2O and O_2 contents less than 1 ppm.

Morphology studies using scanning electron microscopy (SEM)

Microstructural characterization of $LiRhO_2$, $Li_{0.5}RhO_2$ and Li_0RhO_2 was performed by means of scanning electron microscopy (SEM) with a Leo 1530 Gemini electron microscope (Zeiss/Leo) equipped with a Bruker Inlens detector at an acceleration voltage of 20 kV.

For SEM measurements, Li-deficient $Li_{0.5}RhO_2$ and Li_xRhO_2 were prepared in electrochemical cells under charging to 3.85 V and 4.15 V vs. Li^+/Li. A polytetrafluoroethylene (PTFE) condensed liquid binder (5% w/w) was added for preparation of the cathode mixture containing $LiRhO_2$ (85% w/w) and carbon black (10% w/w), which was pressed on Al-meshes with 8 mm diameter and dried in vacuum at 80°C. After charging, they were dissembled in the glovebox; the cathode mixtures were washed by DMC and transferred into the electron microscope.

***In situ* structural investigations during Li-extraction and insertion**

In situ X-ray synchrotron diffraction measurements on $LiRhO_2$ were performed at the synchrotron facility PETRA III/DESY (Hamburg, Germany) at beamline P02.1 in transmission mode using a 16-inch two-dimensional flat panel detector of the XRD 1621 N ES Series (PerkinElmer) with 2048 x 2048 pixels and a pixel size of 200 mm, and a cell setup connected to a VMP multichannel galvanostat [28]. Data were collected in steps of 0.004° over the 2θ-range from 0.1 to 15.4° at a wavelength of 0.20790(1) Å, which was determined from the positions of 8 reflections from a LaB_6 reference material.

In order to characterize the $LiRhO_2$ starting material, a pattern was recorded before the electrochemical process was started. The cell was then successively charged and discharged in galvanostatic mode at a constant current corresponding to the intercalation or deintercalation of 1 Li per formula unit during 10 h (C/10 rate). All diffraction patterns were analyzed by Fullprof implemented into the software package WinPLOTR [29]. The Al-foil as current collector on the cathode side served as an internal standard during the measurements, and the refined lattice parameter of Al provided an independent control of the reliability of the obtained model parameters.

X-ray photoelectron spectroscopy (XPS)

X-ray photoelectron spectroscopy was applied on the initial $LiRhO_2$ and the products with different lithium contents after electrochemical Li extraction. A PHI 5600 CI system with an Al K_α 350 W monochromatized X-ray source and a hemispherical analyzer at a pass energy of 29 eV were used. Cells with the same cathode mixture consisting of $Li_{1-x}RhO_2$, carbon black and PVDF with a mass of about 30 mg were charged to $x \approx 0.5$ and 1.0, and immediately disassembled in the glove-box. In order to remove electrolyte from the surface, the pellets were washed with DMC and scraped. After drying the samples were transferred from the glovebox to the XPS system in an Ar-filled transfer chamber performing in this way a *quasi in situ XPS* analysis [30]. During XPS measurements, when necessary, surface charging was minimized by means of a low-energy electron flood gun. The system base pressure was below 10^{-9} mbar. The binding energy scale was calibrated from minor carbon contaminations using the C1s peak maximum at 284.8 eV.

Structural characterization by transmission electron microscopy (TEM)

The $Li_{1-x}RhO_2$ samples were investigated with selected area electron diffraction (SAED) and electron diffraction tomography (EDT) using an FEI Tecnai G2 electron microscope operated at 200 kV. The samples for the TEM study were prepared by grinding the material in hexane and depositing a few drops of the suspension onto holey carbon TEM grids. The samples were stored and all preparations performed in a glovebox filled with argon. A Gatan vacuum transfer holder was used to prevent exposure of the sample to the air during the transport to the electron microscope. Electron diffraction tomography (EDT) data were collected in the angular range ~ $\pm 40^o$ using manual rotation with a 1^o step, followed by a reciprocal space reconstruction with the PETS software [31]. The positions of rhodium atoms were found by the charge flipping method using the SUPERFLIP program [32]. The atomic coordinates of the oxygen atoms were determined using difference Fourier maps. In order to complete the structure model, it was first refined from electron diffraction data without the Li atoms, using the JANA2006 program [33]. Then, the tentative positions of the Li atoms were obtained by means of Monte Carlo-based optimization, taking into account the anti-bump cost function (preventing short interatomic distances), bond valence sum cost function, and the cost function of the agreement with the electron diffraction intensities. Atomic coordinates of the Rh- and O-atoms

positions were fixed during the optimization to the values obtained in the refinement. The most probable location of the Li atoms was found at the 4*i* tetrahedrally coordinated position.

The cation arrangement in the $Li_yRh_3O_6$ structure was investigated using high resolution high angle annular dark field scanning transmission electron microscopy (HAADF-STEM) images. The data were collected on a probe aberration corrected FEI Titan^3 80-300 microscope operated at 300 kV with a probe convergence semiangle 21 mrad and a beam current about 40 pA.

Density-functional calculations

Stability of different structures formed upon Li deintercalation from $LiRhO_2$ was assessed by density-functional band-structure calculations performed in the VASP code [34, 35] using the Perdew-Burke-Ernzerhof (PBE) flavor of the exchange correlation potential [36]. The PBE+*U* correction with the on-site repulsion U_d = 3 eV and Hund's exchange J_d = 0.5 eV [37, 38] was applied to Rh 4*d* states considering their correlated nature. Spin-polarized calculations were performed converging to the magnetic solutions for Rh^{4+}-containing compounds, whereas Rh^{3+} remained non-magnetic in the low-spin state. Similar results for the phase stability were obtained in spin-unpolarized PBE calculations, although the Rh^{4+}/Rh^{3+} redox potentials were somewhat underestimated, similar to other Li intercalation materials [39, 40]. Both atomic positions and lattice parameters of all structures were relaxed in the calculations.

Acknowledgements

This research has received funding from the BMBF, project grant number 03SF0477B (DESIREE) and has benefitted from beamtime allocation at the High Resolution Powder Diffractometer at beamline P02.1 at the PETRA III synchrotron source (DESY, Hamburg, Germany).

Supporting Information

Detailed crystallographic information of $Li_{1-x}RhO_2$ with different Li-contents, obtained from *in situ* synchrotron powder diffraction data; SAED patterns of the rutile-ramsdellite $Li_yRh_3O_6$ structure; HAADF-STEM images showing the orientation relation between the layered and framework structures; suggested mechanism of the

formation of the [2x2] hollandite-type tunnels in $Li_yRh_3O_6$; thermal stability and thermogravimetric analysis of the rutile-ramsdellite $Li_yRh_3O_6$ compound.

References

(1) Lithium Batteries: Science and Thechnology, Edited by G.-A. Nazri, G. Pistoia, Springer Science + Business Media, 2009, 708 p.

(2) Thackeray, M. M.; Kang, S.-H.; Johnson, C.S.; Vaughey, J.T.; Benedek, R.; Hackney, S. A. *J. Mater. Chem*. 2007, 17, 3112–3125.

(3) Tarascon, J.-M.; Vaughan, G.; Chabre, Y.; Seguin, L.; Anne, M.; Strobel, A P.; Amatucci, G. *J. Solid State Chem*. 1999, 147, 410-420.

(4) Koga, H.; Croguennec, L.; Ménétrier, M.; Mannessiez, P.; Weill, F.; Delmas, C. *J. Power Sources* 2013, 236, 250-258.

(5) Graetz, J.; Ahn, C. C.; Yazami, R.; Fultz, B. *J. Phys. Chem. B* 2003, 107, 2887-2891.

(6) Oishi, M.; Yogi, C.; Watanabe, I.; Ohta, T.; Orikasa, Y.; Uchimoto, Y.; Ogumi, Z. *J. Power Sources* 2015, 276, 89-94.

(7) Koga, H.; Croguennec, L.; Ménétrier, M.; Mannessiez, P.; Weill, F.; Delmas, C.; Belin, S. *J. Phys. Chem. C* 2014, 118, 5700−5709.

(8) Saubanère, M.; McCalla, E.; Tarascon, J.-M.; Doublet, M.-L. *Energy Environ. Sci*., 2016, DOI: 10.1039/C5EE03048J.

(9) Sathiya, M.; Rousse, G.; Ramesha, K.; Laisa, C. P.; Vezin, H.; Sougrati, M. T.; Doublet, M-L.; Foix, D.; Gonbeau, D.; Walker, W.; Prakash, A. S.; Ben Hassine, M.; Dupont, L.; Tarascon, J.-M. *Nature Mater*. 2013, 12, 827–835.

(10) Sathiya, M.; Leriche, J.-B.; Salager, E.; Gourier, D.; Tarascon, J.-M.; Vezin, H. *Nature Comm*. 2015, 6, 6276.

(11) Sathiya, M.; Abakumov, A. M.; Foix, D.; Rousse, G.; Ramesha, K.; Saubanère, M.; Doublet, M. L.; Vezin, H.; Laisa, C. P.; Prakash, A. S.; Gonbeau, D.; Van Tendeloo, G.; Tarascon, J.-M. *Nature Mater*. 2015, 14, 230–238.

(12) McCalla, E.; Abakumov, A.M.; Saubanère, M.; Foix, D.; Berg, E.J.; Rousse, G.; Doublet, M.-L.; Gonbeau, D.; Novák, P.; Van Tendeloo, G.; Dominko, R.; Tarascon, J.-M. *Science*, 2015, 350, 1516-1521.

(13) Zwicker, W. K.; Groeneveld Meijer, W. O. J.; Jaffe, H. W. *Amer. Mineral*. 1962, 47, 246-266.

(14) Turner, S.; Buseck, P. R. *Nature* 1983, 304,143-146.

(15) Akimoto, J.; Gotoh, Y.; Oosawa, Y. *J. Solid State Chem*. 1997, 129, 7-11.

(16) Grey, I. E.; Cranswick, L. M. D.; Li, C.; Bursill, L. A.; Peng, J.-L. *J. Solid State Chem.* 1998, 138, 74-86.

(17) Zhou, Y.-N.; Ma, J.; Hu, E.; Yu, X.; Gu, L.; Nam, K.-W.; Chen, L.; Wang, Z.; Yang, X.-Q. *Nature Comm*. 2014, 5, 5381.

(18) Kumada, N.; Muramatu, S.; Muto, F.; Kinomura, N. *J. Solid State Chem*. 1988, 73, 33-39.

(19) Mikhailova, D.; Bramnik, N. N.; Bramnik, K. G.; Reichel, P.; Oswald, S.; Senyshyn, A.; Trots, D. M.; Ehrenberg, H. *Chem. Mater*. 2011, 23, 3429–3441.

(20) Baudrin, E.; Cassaignon, S.; Koelsch, M.; Jolivet, J.-P.; Dupont, L.; Tarascon, J.-M. *Electrochem. Comm*. 2007, 9, 337–342.

(21) Shannon, R. D. *Acta Cryst.* A, 1976, 32**,** 751-762.

(22) Nefedov, V. I.; Firsov, M. N.; Shaplygin, I. S. *J. Electron Spectrosc. Relat. Phenom*. 1982, 26, 65-78.

(23) Vallet, C. E.; Choudhury, A.; Sobol, P. E.; White, C. W. *Electrochim. Act*a 1993, 38, 1313-1320.

(24) Dupin, J.-C.; Gonbeau, D.; Vinatier, P.; Levasseur, A. *Phys. Chem. Chem. Phys*. 2000, 2, 1319-1324.

(25) Dahéron, L.; Dedryvère, R.; Martinez, H.; Ménétrier, M.; Denage, C.; Delmas, C.; Gonbeau, D. *Chem. Mater*. 2008, 20, 583-590.

(26) Sathiya, M.; Ramesha, K.; Rousse, G.; Foix, D.; Gonbeau, D.; Prakash, A. S.; Doublet, M. L.; Hemalatha, K.; Tarascon, J.-M. *Chem. Mater*. 2013, 25, 1121-1131.

(27) Springborg, J.; Zehnder, M. *Helvet. Chim. Acta* 1984, 67, 2218-2225.

(28) Herklotz, M.; Scheiba, F.; Hinterstein, M.; Nikolowski, K.; Knapp, M.; Dippel, A.-C.; Giebeler, L.; Eckert, J.; Ehrenberg, H. *J. Appl. Cryst.* 2013, 46, 1117-1127.

(29) Roisnel, T.; Rodriguez-Carvajal, *J. Mater. Sci. Forum* 2001, 378-381, 118-123.

(30) Oswald, S.; Nikolowski, K.; Ehrenberg, H. *Anal. Bioanal. Chem*. 2009, 393, 1871–1877.

(31) Palatinus, L. (2011). PETS – program for analysis of electron diffraction data. Prague: Institute of Physics of the AS CR.

(32) Palatinus, L. *Acta Cryst. A* 2004, 60, 604–610.

(33) Petricek, V.; Dusek, M.; Palatinus, L. *Z. Kristallogr*. 2014, 229, 345-352.

(34) Kresse, G.; Furthmüller, J. *Comput. Mater. Sci*. 1996, 6, 15 (1996).

(35) Kresse, G.; Furthmüller, J. *Phys. Rev. B* 1996, 54, 11169.

(36) Perdew, J. P.; Burke, K.; Ernzerhof, M. *Phys. Rev. Lett*. 1996, 77, 3865.

(37) Luo, Y.; Cao, C.; Si, B.; Li, Y. Bao, J.; Guo, H.; Yang, X.; Shen, C.; Feng, C.; Dai, J.; Cao, G.; Xu, Z. *Phys. Rev. B* 2013, 87, 161121(R).

(38) Mazin, I. I.; Manni, S.; Foyevtsova, K.; Jeschke, H. O.; Gegenwart, P.; Valenti, R. *Phys. Rev. B* 2013, 88, 035115.
(39) Zhou, F.; Marianetti, C. A.; Cococcioni, M.; Morgan, D.; Ceder, G. *Phys. Rev. B* 2004, 69, 201101(R).
(40) Zhou, F.; Cococcioni, M.; Kang, K.; Ceder, G. *Electrochem. Comm*. 2004, 6, 1144–1148.

For Table of Contents Only

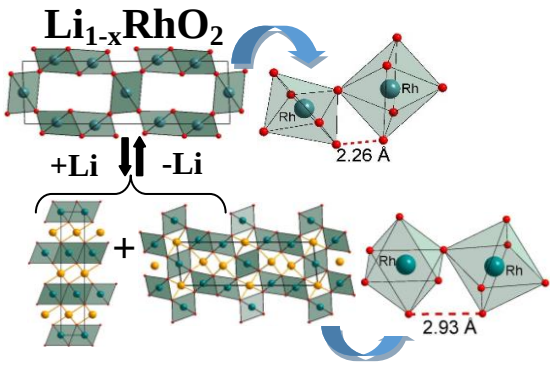

Upon chemical or electrochemical oxidation, layered $LiRhO_2$ shows a unique structural transformation that involves both cation migration and oxidation of oxygen resulting in a stable tunnel-like rutile-ramsdellite intergrowth $Li_yRh_3O_6$ structure. This structure demonstrates excellent performance with the steady and reversible capacity of about 200 mAh/g. The stability of $Li_yRh_3O_6$ is rooted in the accommodation of partially oxidized oxygen species through the formation of short O–O distances that are compatible with the connectivity of RhO_6 octahedra.